J. Phys. B: At. Mol. Opt. Phys. **41** (2008) 074021 (11pp) doi:10.1088/0953-4075/41/7/074021

On the diversity of multiple optimal controls for quantum systems

O M Shir[1], V Beltrani[2], Th Bäck[1], H Rabitz[2] and M J J Vrakking[3]

[1] Natural Computing Group, Leiden University, Niels Bohrweg 1, 2333CA Leiden, The Netherlands
[2] Department of Chemistry, Princeton University, Princeton, NJ 08544, USA
[3] FOM-Institute for Atomic and Molecular Physics (AMOLF), Kruislaan 407, 1098SJ Amsterdam, The Netherlands

Received 14 November 2007, in final form 13 February 2008
Published 25 March 2008
Online at stacks.iop.org/JPhysB/41/074021

Abstract
This study presents simulations of optimal field-free molecular alignment and rotational population transfer (starting from the $J = 0$ rotational ground state of a diatomic molecule), optimized by means of laser pulse shaping guided by evolutionary algorithms. Qualitatively different solutions are obtained that optimize the alignment and population transfer efficiency to the maximum extent that is possible given the existing constraints on the optimization due to the finite bandwidth and energy of the laser pulse, the finite degrees of freedom in the laser pulse shaping and the evolutionary algorithm employed. The effect of these constraints on the optimization process is discussed at several levels, subject to theoretical as well as experimental considerations. We show that optimized alignment yields can reach extremely high values, even with severe constraints being present. The breadth of optimal controls is assessed, and a correlation is found between the diversity of solutions and the difficulty of the problem. In the pulse shapes that optimize dynamic alignment we observe a transition between pulse sequences that maximize the initial population transfer from $J = 0$ to $J = 2$ and pulse sequences that optimize the transfer to higher rotational levels.

(Some figures in this article are in colour only in the electronic version)

1. Introduction

In the last few years, studies of quantum dynamics in atomic and molecular systems under the influence of (intense) femtosecond laser light have increasingly moved from observation of the systems to their control and manipulation. As a result, a number of qualitatively different quantum control schemes can presently be distinguished. Brumer and Shapiro proposed the use of multi-colour interference to control quantum systems [1]. Combinations of harmonic light fields (typically $(\omega, 2\omega)$ or $(\omega, 3\omega)$) can be used to control the total and differential cross-sections of photo-ionization and dissociation processes as well as, recently, the formation of attosecond laser pulses [2]. Whereas the scheme of Brumer and Shapiro emphasizes a frequency-domain description of the quantum system, Tannor and Rice proposed quantum control based on exploiting the time evolution of wave packets that are produced when quantum systems interact with short laser pulses [3]. By using a short pump pulse to prepare a wave packet and a suitably chosen 'dump' pulse to steer the wave packet towards a desired final state, processes such as retinal isomerization of bacteriorhodopsin have been successfully controlled [4]. As a special case of pump-dump control, we may consider the highly successful STIRAP (STImulated Rapid Adiabatic Passage) technique, where population transfer is achieved with unit efficiency by means of a counter-intuitive pump and dump pulse sequence [5]. Finally, Rabitz introduced the concept of feedback control, where phase, amplitude and/or polarization shaping under the influence of a learning loop are used to guide a quantum system towards a desired final state [6]. Many examples exist where this technique has been successfully applied, ranging from the control of chemical reactions [7], selective bond dissociation and molecular rearrangement in the gas phase [8] to photo-excitation of dye molecules in the liquid phase [9], and from control of the energy flow in light harvesting [10] and optimization of the coherent emission of high-harmonic soft x-rays [11] to the energy deposition in high intensity laser–cluster interactions [12].

An important question in relation to quantum control is whether or not the approach allows full control of the quantum system at hand. A few years ago, Rabitz and co-workers reported an analysis of the search landscape that is encountered when feedback control is applied to a quantum mechanical problem. They concluded that controllable quantum systems with no constraints placed on the controls only have extrema that correspond to perfect control or to no control at all [13]. In other words, in a controllable quantum system, when no constraints are placed on the time-dependent light field that interacts with a system, feedback control will drive the system towards the desired result with unit efficiency. This is a remarkable conclusion, since it differs considerably from the intuitive notion of feedback-control experiments as an evolutionary walk through a mountainous landscape with peaks of varying height, where a limited number of peaks might correspond to the desired result and where a large number of lesser peaks can act as traps where the optimization may get stuck.

The difference between Rabitz' 'perfect' result and the notion that common feedback-control experiments may suffer sub-optimal outcome is due to the fact that the observable landscape of a controllable quantum system has no traps. Attaining perfect control then requires that there are no *significant* constraints on the applied field. Practical realizations of feedback control will always be subject to constraints, but whether that will limit attainment of perfect control is generally not *a priori* evident. When feedback-control experiments are performed in the laboratory, the available laser pulses have a finite bandwidth and pulse energy, and additional limits exist on the ability of pulse shapers to introduce desired variations in the spectral amplitude, phase and/or polarization of the frequency components in the laser pulse [14, 15]. Furthermore, the search algorithm that is employed in the feedback loop determines the exploration of the search space and may introduce a bias that prevents the exploration of crucial regions.

In this paper, we explore the influence of some constraints on the outcome of experiments that are performed using feedback control and explore to what extent the conclusions of [13] are upheld when constraints prevent the system from reaching its pre-defined goal. Quantum control objectives are generally underposed with a given starting state and prescribed final objective, but with no detailed guidance on the path between these extremes. This situation suggests that multiple functionally equivalent controls meeting the same objective value should exist. This point has been argued formally [38] and illustrated recently [39–41], with algorithms honed for this purpose. To examine these matters further, we use a computational approach, where constraints that are normally encountered in the laboratory are incorporated in a computer simulation. The quantum system is a rigid diatomic molecule subjected to a linearly polarized laser pulse. We consider two desired outcomes of the laser–molecule interaction: either (a) alignment of the angular distribution of the molecule along the laser polarization axis after the laser–molecule interaction is over (field-free molecular alignment) [16] or (b) control of rotational population transfer [17]. If the sample of molecules is incoherently distributed over a set of states (e.g., a Boltzmann distribution) that are limited in their ability to achieve a pre-defined goal, then the attainable final yield will be limited as well. In line with our recently established experimental capabilities [18] and in order to simplify the present analysis, we assume that the sample of molecules is initially in the $J = 0$ ground rotational state.

When molecules are exposed to an intense laser, they tend to align their internuclear axis to the polarization axis of the laser [19]. This effect, called dynamic alignment, occurs because the potential energy of the oscillating dipole induced by the laser is minimized when the molecule is aligned. Dynamic alignment occurs in two variants, depending on whether the duration of the laser pulse is long or short compared to the rotational period of the molecule. In the former case, the rotational states of the molecule adiabatically adapt to the laser field, forming pendular states that are aligned along the laser polarization axis [20, 21]. In the latter case, the laser excites a rotational wave packet by impulsive stimulated Raman scattering that leads to an alignment of the molecule both during and at a particular time after the laser pulse. A few years ago field-free alignment was demonstrated in pump-probe experiments on I_2, where the alignment induced by an intense infrared alignment pulse was monitored by means of Coulomb explosion imaging [16]. At well-defined times, given by the rotational period of the molecule, alignment revivals occurred where the angular width suddenly increases or decreases during several picoseconds. This type of field-free alignment is of interest for many applications in physics and chemistry, recent examples being the use of field-free aligned molecules in high-harmonic generation experiments aimed at determining the electronic [22] and nuclear [23] structure of molecules.

The degree of field-free alignment that can be accomplished by a single laser pulse is limited by the maximum intensity that a molecule can be subjected to before competing processes such as ionization and fragmentation take over. Quantum control methods provide an opportunity to search for laser excitation fields that have a lower peak intensity, while maintaining or even improving the degree of alignment that is accomplished. Early work concerned with optimizing the degree of field-free alignment suggested the use of a sequence of laser pulses. As proposed theoretically by Averbukh [24] and subsequently demonstrated numerically by Averbukh and Rabitz [25], as well as experimentally by Stapelfeldt and co-workers [26], field-free alignment can be optimized by using a sequence of pulses where the inter-pulse separation matches the rotational period (or a suitable fraction thereof) of the molecule. This conclusion was also reached in [27] where an evolutionary approach was applied to the optimization of field-free alignment for finite-temperature samples and where optimized pulse shapes consisting of trains of up to five laser pulses were observed. Recent work on the optimization of dynamic alignment using pulse shaping by Pinkham *et al* [28], and by Hertz *et al* [29], explored the possibility of optimizing alignment by means of chirp-induced changes in the laser pulse shape without allowing the pulse to break up into a train with a spacing comparable to the rotational period.

In dynamic alignment, the modification of the angular distribution (usually expressed by means of the expectation value $\langle\cos^2\theta\rangle$, where θ is the angle of the internuclear axis with respect to the polarization axis) is largely determined by the number of rotational states that contribute to the rotational wave packet produced. Hence, optimizing dynamic alignment leads to optimization of the Raman process that produces the wave packet. A related, though different, goal is to request that the optimization leads to transfer of all of the population into a single rotational state. In this case, static field-free alignment will be produced, and—when performed with a sample containing only a single initial rotational state, as is the case here—the laser preparation may serve to produce a state-selected molecular sample. Optimization of the efficiency of rotational population transfer by means of a sequence of two pulses (without accomplishing unit efficiency in the transfer of the population to a single state) was reported recently [17]. In the present paper, both dynamic alignment and population transfer towards a selected rotational state will be considered.

2. Methodology

2.1. Calculating field-free alignment and rotational population transfer

The computational methods for the calculation of time-dependent molecular alignment and rotational population transfer were previously described [30] and used in an evolutionary optimization for a finite-temperature molecular sample [27]. The evolution of the molecule in the laser field is evaluated quantum mechanically by performing calculations where the molecule is considered to consist of an electronic ground state X and a (far off-resonant) excited state A. In contrast with our previous work [27], we will only be concerned with the time-dependent alignment of molecules that initially occupy the $J = m = 0$ rotational state. Hence, the wavefunction is expanded as

$$\Psi(t) = \sum_{J=0}^{N_{\mathrm{ROT}}} (\alpha_{X,J}(t)\psi_{X,J} + \alpha_{A,J}(t)\psi_{A,J}) \tag{1}$$

with $N_{\mathrm{ROT}} = 20$ rotational levels, where $\psi_{X,J}$ correspond to the even Legendre polynomials and $\psi_{A,J}$ correspond to the odd Legendre polynomials. This expansion was confirmed to give converged results in the present calculations. The time dependence of the molecular wavefunction is given by

$$\mathrm{i}\hbar\frac{\mathrm{d}\Psi(t)}{\mathrm{d}t} = H\Psi(t) = \{H_0 + V(t)\}\Psi(t). \tag{2}$$

The Hamiltonian consists of a molecular part H_0 and the interaction with the laser field $V(t)$, given by

$$V(t) = \vec{\mu}\cdot\vec{E}(t)\cos(\omega t). \tag{3}$$

The eigenvalues of H_0 are $E(J) = B_{\mathrm{rot}}J(J+1)$, where $B_{\mathrm{rot}} = 5\ \mathrm{cm}^{-1}$ is the rotational constant of the molecule (the revival time is $T_{\mathrm{rev}} = 1/(2B_{\mathrm{rot}}c) = 3.3$ ps). We note that centrifugal distortion is not taken into account. The laser field induces transitions between the rotational states via subsequent Raman processes. The transitions between X and A proceed via the selection rules $\Delta J = 1$. Inserting equation (1) into equation (2) and applying the rotating-wave approximation (RWA) produces a set of differential equations which can be efficiently solved by diagonalization of the Hamiltonian and propagation in terms of the field-dressed eigenstates. We note that calculations performed using this computational approach on a strongly related problem have confirmed that under the available conditions the rotating-wave approximation does not influence the outcome of the calculation.

The envelope of the laser field (which governs the dynamics in the rotating-wave approximation) is described by

$$E(t) = \mathrm{Re}\int A(\omega)\exp(\mathrm{i}\varphi(\omega))\exp(\mathrm{i}\omega t)\,\mathrm{d}\omega. \tag{4}$$

In the present calculation, the control is the phase function $\varphi(\omega)$. This phase function is either obtained by defining the phase at a set of $N = 80$ or 160 frequencies that are equally distributed across the spectrum of the pulse or is written as a superposition of the first $N_{\mathrm{H}} = 40$ Hermite polynomials, with expansion coefficients that are optimized in the course of the calculation. The spectral function $A(\omega)$ is a Gaussian with a width chosen such that the FWHM length of the Fourier-limited pulse ($\varphi(\omega) = 0$) is 100 fs. Hence, the Fourier-limited pulse duration is much shorter than the rotational period. The intensity of the laser enters the calculation through specification of the peak Rabi frequency Ω_{XA} for the coupling of the X and the A electronic states. The non-resonant detuning of the A state is assumed to be $10^{15}\ \mathrm{s}^{-1}$.

2.2. Optimization strategies

On the basis of earlier work on dynamic alignment starting from finite-temperature samples [27] and due to previous calculations that showed that certain variants of derandomized evolution strategies perform better with respect to other evolutionary algorithms on these problems [33–35], we restrict our study to these state-of-the-art algorithms. There are two simulations with different objectives: (a) the maximization of the $\langle\cos^2\theta\rangle$-alignment that occurs after the laser pulse is over ($t > 12$ ps) during the field-free evolution of the rotational wave packet, subject to a penalty function that prevented the electric field strength in the pulse from exceeding 0.6 of the transform limited value[1] or (b) the maximization of the population transfer towards a selected rotational level as determined at the end of the laser–molecule interaction.

2.2.1. Evolution strategies (ES). Evolution strategies [36] are canonical evolutionary algorithms for continuous function optimization, due to their straightforward real-valued encoding, their specific variation operators as well as due to their high performance on benchmark problems compared to other methods. A task becomes more suitable for an ES when the dimensionality of the search space increases. In evolution strategies, each individual carries, apart from the real-valued

[1] In most of the results presented in this paper the presence of this penalty function did not play a role.

array of search parameters, a vector of strategy parameters, which determines the mutation step size in each direction. Both the search parameters, also referred to as object variables or decision parameters, as well as the strategy parameters are optimized.

2.2.2. Derandomized evolution strategies. Mutative step-size control tends to work well for the adaptation of a global step size, but tends to fail when it comes to the individual step sizes (i.e., variances and covariances of the joint distribution). This is due to several disruptive effects as well as due to the fact that the selection of the strategy parameter settings is indirect [37]. The so-called derandomized mutative step-size control aims to handle those disruptive effects[2]. In our notation, a (μ, λ) strategy refers to a population of μ parents, generating λ offspring, out of which μ are selected based on their ranked yield to become the parents of the following generation.

2.2.3. The (1, λ)-DR2 algorithm. The DR2 algorithm [38] is considered to be the second generation of the derandomized evolution strategies. This variant uses a linear number in the search space dimensionality $\boldsymbol{n}$ of strategy parameters as a strategy vector $\vec{\delta}^{g}_{\mathrm{scal}}$, and it aims to accumulate information about the correlation or anti-correlation of past mutation vectors in order to adapt the step-size $\boldsymbol{\delta}$:

$$\vec{x}^{g+1} = \vec{x}^{g} + \delta^{g} \cdot \vec{\delta}^{g}_{\mathrm{scal}} \cdot \vec{Z} \tag{5}$$

where $\vec{Z}$ is the mutation vector, i.e. an array of random variables that are drawn from a normal distribution. In each generation, the best solution generated by the mutation operator is retained and becomes the seed for the next generation, $\vec{x}^{g}$.

2.2.4. The (μ, λ) covariance matrix adaptation (CMA-ES). The (μ, λ)-CMA-ES algorithm [37] is known as the state-of-the-art among the derandomized ES variants. It has been successful for treating correlations among object variables, where it applies principal component analysis (PCA) to the selected mutations during the evolution for the adaptation of the covariance matrix of the distribution, $C^{g} \in \Re^{n \times n}$:

$$\vec{x}^{g+1} = \vec{x}^{g} + \sigma^{g} \cdot B^{g} \cdot D^{g} \cdot \vec{Z} \tag{6}$$

where the covariance matrix is eigenvalue-decomposed as

$$C^{g} = B^{g} \cdot D^{g} \cdot (B^{g} \cdot D^{g})^{T}. \tag{7}$$

Thus, it learns a full covariance matrix during the course of evolution. We note that the number of strategy parameters in CMA-ES is quadratic in $\boldsymbol{n}$.

[2] It is important to note that the particular variants of derandomized ES are subject to different numbers of strategy parameters for adaptation, and this affects the efficiency of the optimization: it is either of *linear* or *quadratic* order in terms of the dimensionality of the search problem $\boldsymbol{n}$, and there is a trade-off between the number of strategy parameters and the time needed for the adaptation/learning process of the step sizes. The choice is up to the user, who should fit the strategy to the specific nature of the search problem.

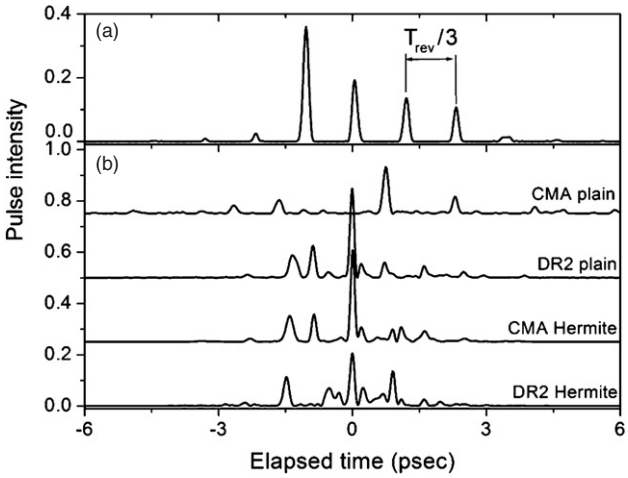

Figure 1. (a) Comparison of an optimization performed using the DR2 algorithm with $\Omega_{\mathrm{XA}} = 40 \times 10^{12}\ \mathrm{s}^{-1}$ and (b) four calculations with $\Omega_{\mathrm{XA}} = 160 \times 10^{12}\ \mathrm{s}^{-1}$ employing the DR2 algorithm and the CMA algorithm with either a simple (plain) point-by-point specification of $\varphi(\omega)$ or a specification of $\varphi(\omega)$ as a superposition of Hermite polynomials. The four calculations shown are the best results out of 20 trials for each approach.

3. Optimization of dynamic alignment

3.1. Optimizations using a fixed laser pulse energy

Optimization of field-free molecular alignment starting from $J = 0$ was performed for a number of algorithmic approaches. In each case, the same calculation was attempted 20 times, with different random values of the initial trial solution. Each run was limited to 20 000 function evaluations. In this section, the discussion is restricted to the best results obtained in each series of 20 trials.

In figure 1 a comparison is shown between one optimization of dynamic alignment starting from $J = 0$, performed using the DR2 algorithm under perturbative conditions ($\Omega_{\mathrm{XA}} = 40 \times 10^{12}\ \mathrm{s}^{-1}$) and four optimizations performed under non-perturbative conditions ($\Omega_{\mathrm{XA}} = 160 \times 10^{12}\ \mathrm{s}^{-1}$) using both the CMA and the DR2 algorithm, with either a point-by-point definition of the phase function $\varphi(\omega)$ (henceforth called a plain parameterization) or a definition of $\varphi(\omega)$ in terms of a superposition of the first $N_{\mathrm{H}} = 40$ Hermite polynomials. These values of the parameter settings gave the best trade-off between field resolution and optimization efficiency. Furthermore, based on past experience, we chose a (1, 10) strategy for the DR2 algorithm. When using the CMA method with the Hermite polynomials ($N_{\mathrm{H}} = 40$) we used a (7, 15)-strategy, and using the CMA method with the point-by-point definition of the phase ($n = 80$) an (8, 17)-strategy was used.

At low laser intensity ($\Omega_{\mathrm{XA}} = 40 \times 10^{12}\ \mathrm{s}^{-1}$) the result is simple. A pulse train is observed where the spacing between the peaks is approximately the rotational period of a coherent superposition state consisting of $J = 0$ and $J = 2$ only ($T_{\mathrm{rev},02} = 1/(6B_{\mathrm{rot}}c) = 1.1$ ps). The time-dependent intensity is given by a train of pulses where the largest pulse reaches an intensity of 0.36 I_{FTL}, where I_{FTL} is the peak intensity of

Table 1. Largest expectation value $\langle\cos^2\theta\rangle$ encountered in 20 trials with the CMA and DR2 algorithms used in combination with different parameterizations of $\varphi(\omega)$. The optimizations were performed using a laser bandwidth corresponding to a 100 fs Fourier-limited pulse and peak Rabi frequency of 160×10^{12} s^{-1}.

	CMA	DR2
Plain	0.945	0.962
Hermite	0.961	0.957

the Fourier-limited pulse, due to the fact that the algorithm has applied a penalty to pulses containing features with an intensity larger than this value.

At high laser intensity ($\Omega_{XA} = 160 \times 10^{12}$ s^{-1}), the pulse shapes determined are considerably more complex and no simple periodicity can be observed. The largest values of $\langle\cos^2\theta\rangle$ obtained are shown in table 1. The two cases with the largest alignment are with the CMA algorithm in combination with a parameterization utilizing Hermite polynomials or with the DR2 algorithm using plain parameterization. Use of the CMA algorithm with the plain parameterization or the DR2 algorithm with the Hermite parameterization yields a slightly lower value over 20 trials. Based on our experience with the problem and the algorithms, the yield differences of table 1 are believed to be significant. This is supported by inspection of the pulse shapes shown in figure 1. The two most successful optimizations (CMA/Hermite and DR2/Plain) not only share their value of $\langle\cos^2\theta\rangle$, but furthermore make use of a pulse shape that is very similar. While this does not constitute a proof, we speculate that within the constraints in the optimization (i.e., the finite pulse bandwidth and energy, as well as the finite resolution of the phase function) both algorithms have found a solution that approaches the best solution that is possible. However, even if the solutions are optimal within the constraints set by the laser bandwidth, the laser pulse energy and the parameterization of the phase, it is clear that the solutions do not approach the maximum alignment that can be supported by the basis of 20 rotational states (see equation (1)) that were used in the calculation. The maximum alignment supported by this basis is the largest eigenvalue of the observable matrix, which was found to be 0.9863. The corresponding eigenvector will be referred to here as the maximal eigenvector or the maximal wave packet.

We ascribe the difference between this maximum value and the values obtained in the optimizations as being largely due to the finite laser bandwidth in our calculations. The bandwidth and the pulse duration of a laser pulse with a Gaussian shape are related by

$$\Delta\omega_{\text{laser,FWHM}} \times \tau_{\text{laser,FWHM}} \geqslant 2\pi c_B \tag{8}$$

where $c_B = 0.441$. For a pulse with a 100 fs Fourier-limited duration, the bandwidth is $\Delta\omega_{\text{laser,FWHM}} = 0.0182$ eV $= 147$ cm^{-1}. When a molecule undergoes a Raman transition from $J = J_0$ to $J = J_0 + 2$, the energy absorbed from the laser field is $B_{\text{rot}}(4J_0 + 6)$. This absorbed energy is the difference between the pump and dump photons involved in the Raman excitation. Consequently, the Raman excitation becomes frustrated when $B_{\text{rot}}(4J_0 + 6) > \Delta\omega_{\text{laser,FWHM}}$. In our case,

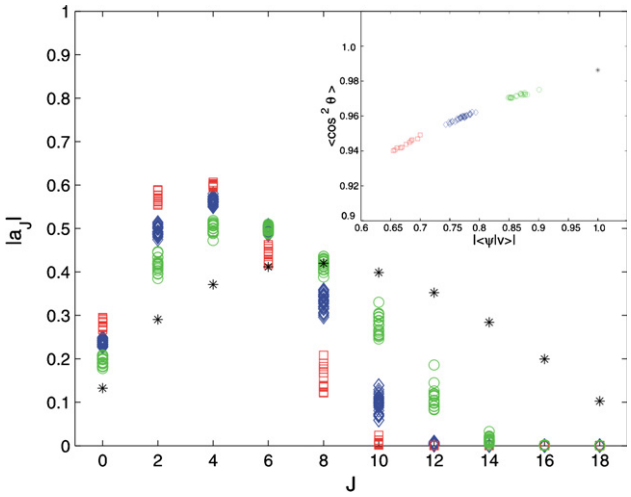

Figure 2. The distribution of the maximal and the best optimized wave packets over the rotational states. Black stars represent the maximal wave packet in the finite rotational basis (i.e., corresponding to the highest-ranked eigenvector of the observable matrix). Blue diamonds represent the 1st optimized set of solutions (CMA-Hermite/DR2-Plain) and red squares represent the 2nd optimized set of solutions (CMA-Plain/DR2-Hermite); green circles represent calculations with doubled bandwidth and the same fluence (50 fs pulse with $\Omega_{XA} = 226 \times 10^{12}$ s^{-1}), optimized by the DR2 with plain parameterization. The figure clearly shows that the limited field bandwidth cuts off the rotational states for the optimized solutions after $J = 10$, when the original bandwidth is used or after $J = 12$ when the bandwidth is doubled. Furthermore, this plot illustrates the distinction between the two families of solutions for the original bandwidth (i.e., blue diamonds and red squares) arising from the different algorithms. Inset: the alignment as a function of the overlap of the optimized wave packets $|\psi\rangle$ with the maximal eigenvector $|V\rangle$. Note that the overlap for the original bandwidth never exceeds 0.8 in magnitude. Also note the three clusters for the families of algorithmic solutions.

with a rotational constant of $B_{\text{rot}} = 5$ cm^{-1}, this threshold occurs for $J_0 \approx 6$. As figure 2 shows, the rotational wave packet that displays the largest alignment after the optimization contains only limited contributions from $J = 8$ and $J = 10$, and none from rotational levels above $J = 10$. By contrast, the maximal wave packet that is supported by the rotational basis used in the calculations contains contributions all the way up to $J = 18$. In this respect, it may appear to be surprising that a high yield of 0.962 can be obtained when the optimized wave packet differs so much from the maximal wave packet. In order to assess the crucial influence of the bandwidth constraint on the cut-off of accessible J values, additional calculations were performed with the original bandwidth doubled while the fluence was kept fixed (thus corresponding to a 50 fs pulse with $\Omega_{XA} = 226 \times 10^{12}$ s^{-1}). These results are also presented in figure 2 for comparison to the calculations with the original bandwidth. The doubling of the bandwidth permitted populating up to $J = 12$, and thus produced an enhanced alignment yield of 0.975.

The difference between the maximally attainable wave packet and that obtained by the optimization is also reflected in the angular probability distribution functions pictured in figure 3. These probability distribution functions are

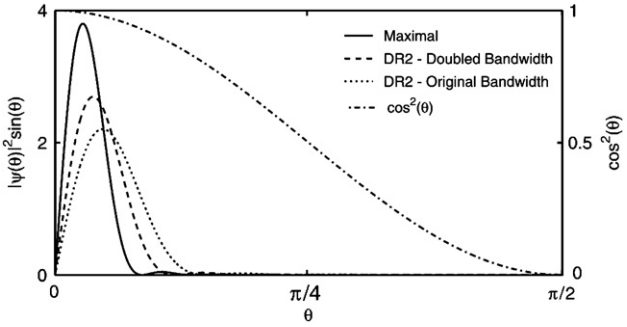

Figure 3. Left axis: normalized angular probability distribution function for the maximal case $|\psi_{\max}(\theta)|^2 \sin(\theta)$ and the optimized control function $|\psi_{\text{opt}}(\theta)|^2 \sin(\theta)$. Right axis: the value of $\cos^2(\theta)$. The constraints prohibit the evolutionary algorithm from attaining the absolute maximal angular probability distribution function; however, the expectation value of the observable $\langle\cos^2(\theta)\rangle_{\text{opt}} = 0.9621$ when using the original bandwidth corresponding to a 100 fs Fourier-limited pulse is within 0.025 of the maximum attainable value $\langle\cos^2(\theta)\rangle_{\max} = 0.9863$. When doubling the bandwidth (i.e. basing the shaped laser pulse on a 50 fs Fourier-limited pulse) $\langle\cos^2(\theta)\rangle_{\text{opt}}$ increases to 0.975, which is only 0.0113 away from the maximum attainable value.

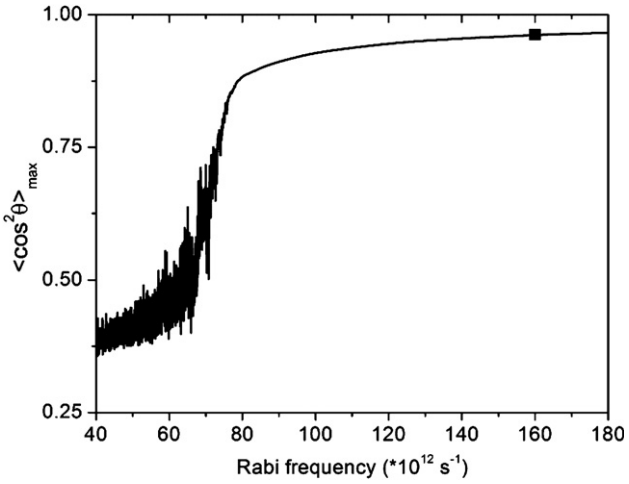

Figure 4. Observed alignment in an optimization employing the DR2 algorithm and a plain parameterization of the phase function at 160 frequencies where the laser intensity was linearly varied during the optimization process. After an initial learning stage, the optimization produces a high degree of alignment and accomplishes $\langle\cos^2\theta\rangle = 0.962$ when Ω_{XA} reaches a value of 160×10^{12} s^{-1}, very similar to the results shown in figure 1 (square).

respectively constructed from the coefficients of the maximal eigenvector as well as the state obtained from the optimized field, based on equation (1). Even though at the higher bandwidth the discrepancy between the optimally controlled distribution function and the maximally attainable limit appears to be significant, a high alignment value was still obtained. The explanation for this excellent behaviour, despite considerable differences in the composition of the wavefunction, lies in the variational principle [42] which states that a first-order error in a trial wavefunction (i.e., the wave packet from the bandwidth limited optimal control field) will produce an extremum eigenvalue (i.e., the alignment) of second-order error.

When a molecule is exposed to a shaped, intense laser pulse the optimization has to accomplish two things. First, the optimization has to create a wave packet consisting of a large number of rotational states that can serve to align the molecule. Second, the optimization has to prepare the wave packet with the correct phase relationship between the component wavefunctions, so that during its field-free evolution these components coherently add up to generate an optimally aligned wavefunction. While there is no criterion available that allows us to ascertain whether the algorithm has optimized the population distribution, it is possible to investigate the phase relationship of the component wavefunctions in the optimized solutions. Maximum alignment occurs if at some point in time the phases of all component wavefunctions differ from each other by 0 (modulo 2π). Separate inspection of the wave packets that correspond to the pulses given in figure 1 (but not visualized here) reveals that the algorithm produces the wave packet with a relative RMS phase error of only 0.0566 rad. While we cannot establish whether the optimization has distributed the population in the best possible way, we do observe that the algorithm has properly phased all component wavefunctions with respect to each other. This type of coherent alignment of phases was also observed to be optimal in the mechanistic analysis of another state-to-state control application [39].

3.2. Optimization of dynamic alignment starting from $J = 0$ with a generation-dependent laser intensity

In order to observe, and possibly understand how the optimal laser pulse shape evolves from the simple pulse train observed for $\Omega_{\text{XA}} = 40 \times 10^{12}$ s^{-1} (figure 1(a)) into a much more complicated pulse shape for $\Omega_{\text{XA}} = 160 \times 10^{12}$ s^{-1} (figure 1(b)), a series of calculations were performed where Ω_{XA} was increased linearly as a function of the generation number. In these calculations, the molecule was initially exposed to a shaped laser field with $\Omega_{\text{XA}} = 40 \times 10^{12}$ s^{-1}, and over 10^4 generations this value linearly increased to a $\Omega_{\text{XA}} = 180 \times 10^{12}$ s^{-1}. Figure 4 shows that after an initial stage where the algorithm learned about the properties of the search landscape, a smooth increase is observed in $\langle\cos^2\theta\rangle$ as a function of intensity. Upon proper tuning of the optimization (including switching to a search problem of 160 decision parameters, rather than only 80) the best $\langle\cos^2\theta\rangle$ value from figure 1 could be recovered: a $\langle\cos^2\theta\rangle$ value of 0.962 (i.e., the value as in table 1, to three decimal places) was obtained when Ω_{XA} was equal to 160×10^{12} s^{-1}.

In figure 5, the pulse shape that the algorithm employed at $\Omega_{\text{XA}} = 160 \times 10^{12}$ s^{-1} is compared to the optimum pulse shape previously shown in figure 1. Several conclusions can be drawn from figure 5. While the value of $\langle\cos^2\theta\rangle$ is the same for both calculations (as well as in further calculations using this approach), the pulse shapes are very different. Evidently, although the actual value of $\langle\cos^2\theta\rangle$ hardly differs, the pulse shape that the algorithm finds is heavily influenced by the way that the adaptation of the pulse intensity steered the

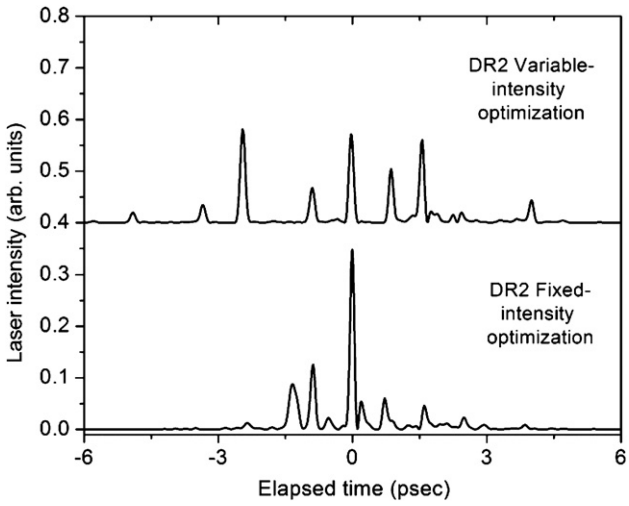

Figure 5. Comparison of pulse shapes that were obtained in optimizations employing the DR2 algorithm, when using a fixed $\Omega_{XA} = 160 \times 10^{12}\ s^{-1}$ (bottom, see figure 1) or—at this same value of Ω_{XA}—in the course of an optimization where Ω_{XA} was linearly varied from $40 \times 10^{12}\ s^{-1}$ to $180 \times 10^{12}\ s^{-1}$ (see figure 4).

calculations through the search landscape. This behaviour is consistent with formal analysis of control landscapes and their *level sets* [13, 40, 41]. A control level set consists of the family of control fields that produce the same value of the observable.

Next, we explore how the solutions evolve when the intensity is varied. Calculations were performed where the intensity was first ramped from low-to-high (involving a learning process as in figure 4), before reversing the process and bringing the intensity back down. Since in the latter part of the procedure the optimization starts from a converged result, highly optimized solutions can be maintained throughout the excursion, and the transition from high-to-low intensity can be continuously observed. Figure 6 shows an example of this procedure. A sequence of pulses are shown, starting from the pulses (at low intensity) near the bottom, where the learning process takes place, moving up to the centre of the plot where the intensity is maximal, before reducing to a lower intensity again for the pulses shown in the upper part of the plot. These latter pulse shapes are a very simple pulse train, with a pulse separation of 2.2 ps (i.e. $1/3B_{rot}c$). This pulse train is very different from the pulse train in figure 1, where a pulse separation of 1.1 ps was observed in the calculation where Ω_{XA} was constrained at a value of $40 \times 10^{12}\ s^{-1}$ Nevertheless, the alignment observed at the end of the optimization of figure 6 reaches a value of $\langle \cos^2\theta \rangle = 0.548$, which compares rather well with the value of 0.550 found in figure 1. At these low intensities, as previously observed at high intensity, vastly different pulse shapes are able to produce similar optimized values of $\langle \cos^2\theta \rangle$. These solutions are on a level set, but the present calculations do not reveal if these solutions are on connected (i.e., continuously morphable from one level set to another) or disconnected components of the level set [42].

At low intensity the $1/(6B_{rot}c) = 1.1$ ps period observed in figure 1 and the $1/(3B_{rot}c) = 2.2$ ps period observed in

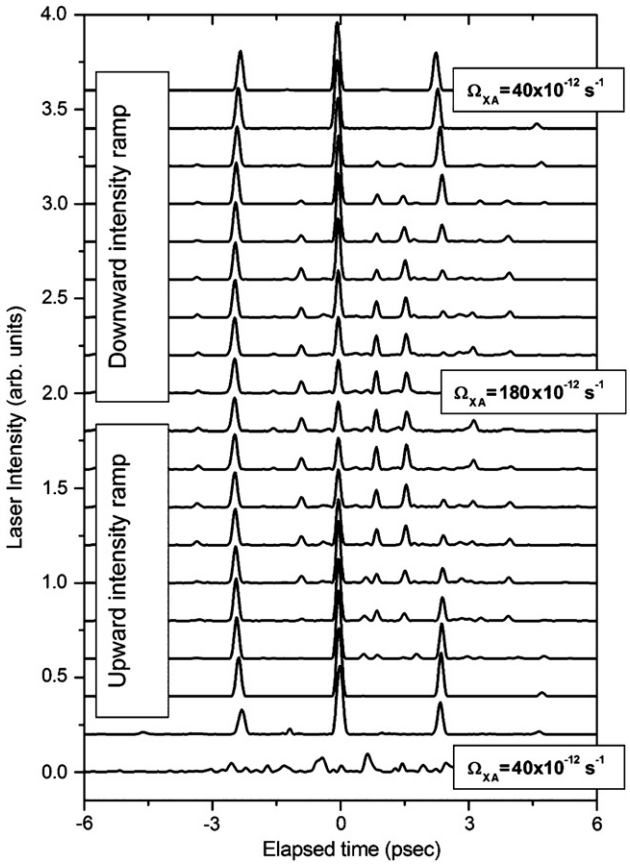

Figure 6. Evolution in the normalized pulse shapes encountered in an optimization employing the DR2 algorithm, where Ω_{XA} was first linearly varied from $40 \times 10^{12}\ s^{-1}$ to $180 \times 10^{12}\ s^{-1}$ and then back down to $40 \times 10^{12}\ s^{-1}$. A smooth evolution in the normalized pulse shapes is observed, which at the end of the procedure leads to a pulse at $40 \times 10^{12}\ s^{-1}$ which is significantly different from the pulse shown in figure 1, which was obtained in a calculation with a fixed value of Ω_{XA}.

figure 6 correspond to a laser interaction that occurs once per period $T_{rev,02} = 1/(6B_{rot}c) = 1.1$ ps of the $J = (0, 2)$ coherent superposition state (figure 1) or every 2nd period (figure 6). This can clearly be seen in figure 7, where the temporal behaviour is shown for the laser pulse shape and the induced dynamic alignment for $\Omega_{XA} = 54 \times 10^{12}\ s^{-1}$, $110 \times 10^{12}\ s^{-1}$ and $166 \times 10^{12}\ s^{-1}$ As the intensity is increased, higher rotational states begin to contribute to the rotational wave packet and the $T_{rev} = 1/(2B_{rot}c) = 3.3$ ps rotational period begins to assert itself, as a consequence of the energy differences between rotational levels J_0 and $J_0 + 2$ being multiples of $2B_{rot}$ for all values of J_0. In the latter half of the pulse ($t > 0$), additional narrowly spaced pulses come into play that are spaced by $T_{rev}/4 = 1/(8B_{rot}c) = 0.8$ ps. The occurrence of these new peaks comes at the expense of the peak at 2.2 ps, which is considerably weakened in the calculation at $\Omega_{XA} = 110 \times 10^{12}\ s^{-1}$ (b) and completely absent in the calculation at $\Omega_{XA} = 166 \times 10^{12}\ s^{-1}$ (c). In the latter calculation a new peak has appeared at a delay of 3.3 ps, corresponding to the full revival of the rotational wave packet formed. Hence, we conclude that the optimum pulses observed in the simulations

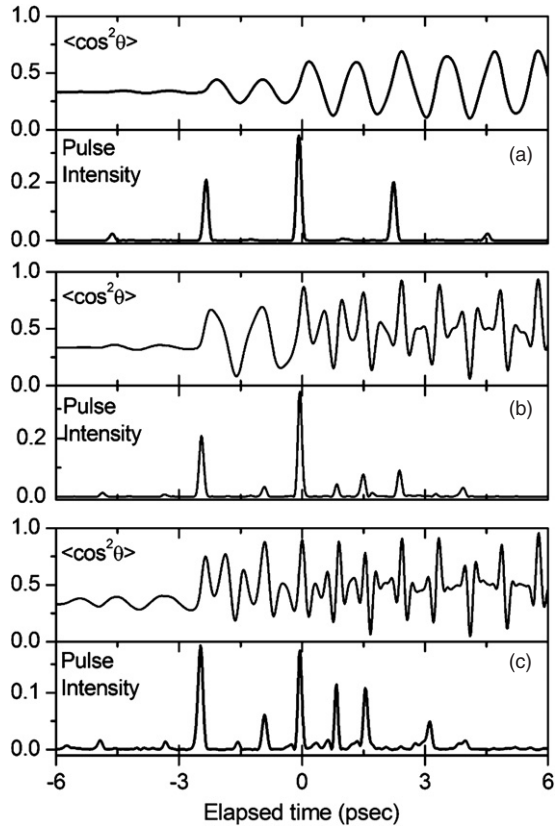

Figure 7. Intensity dependence of the alignment $\langle\cos^2\theta\rangle$ and the laser pulse shape from an optimization where the laser intensity Ω_{XA} was first increased from 40×10^{12} s^{-1} to 160×10^{12} s^{-1}, before being tuned back down to 40×10^{12} s^{-1}. The three calculations shown were performed while Ω_{XA} was decreased and correspond to calculations where Ω_{XA} was equal to (a) 54×10^{12} s^{-1}, (b) 110×10^{12} s^{-1} and (c) 166×10^{12} s^{-1}, respectively.

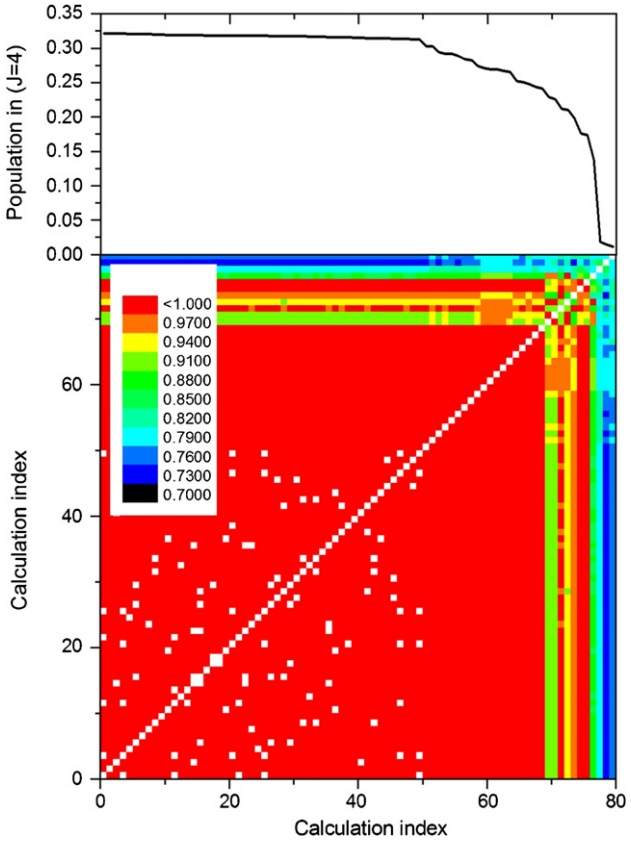

Figure 8. Population transfers from $J = 0$ to $J = 4$ obtained in 80 optimizations performed with the DR2 algorithm with $\Omega_{XA} = 80 \times 10^{12}$ s^{-1} (top), along with the correlation coefficient between these solutions, defined by equation (8) (bottom). The solutions that perform best are highly correlated. Pixels in white correspond to cross-correlation which (after rounding off) are equal to 1.

arise as a result of an interplay between the temporal structure that is required to optimize the transfer from $J = 0$ to $J = 2$, leading to peak separations that are a multiple of $1/(6B_{rot}c)$, and the temporal structure that is required to optimize the transfer from there to higher rotational levels, which leads to peak separations that are multiples of $1/(8B_{rot}c)$.

4. Optimization of rotational population transfer

Optimizations were also performed for population transfer from $J = 0$ to $J = 4$. These optimizations were performed using the DR2 algorithm and for three values of Ω_{XA} (80×10^{12} s^{-1}, 120×10^{12} s^{-1} and 160×10^{12} s^{-1}). All calculations considered the plain parameterization only, and were repeated 80 times, with 10 000 function evaluations per run. Qualitatively different results were obtained for the three intensities considered. For $\Omega_{XA} = 80 \times 10^{12}$ s^{-1} the optimizations were unable to accomplish the transfer from $J = 0$ to $J = 4$ with unit efficiency. The best efficiency obtained was ∼32%. For $\Omega_{XA} = 120 \times 10^{12}$ s^{-1} and for $\Omega_{XA} = 160 \times 10^{12}$ s^{-1} the transfer efficiency approached 100% in most of the calculations.

In order to be able to compare the results of individual optimizations, we define a correlation coefficient that compares the pulse shape used in two calculations i and j as

$$C_{i,j} = \mathrm{Max}(\Sigma_t f_i(t) f_j(t + \Delta t))/[\sqrt{(\Sigma_t f_i(t)^2)}\sqrt{(\Sigma_t f_j(t)^2)}] \quad (9)$$

where $f_i(t)$ and $f_j(t)$ are the field intensities of the pulses obtained in calculations i and j, respectively, and where taking the maximum as a function of Δt reflects that the pulse shapes determined by the optimization may be shifted with respect to each other. The sums are over the discrete time steps in the numerical calculation. According to equation (9) $C_{i,i} = 1$ and $C_{i,j} = 0$ if pulses i and j do not overlap at all.

In figure 8, the correlation coefficient is plotted for the 80 optimizations that were performed for $\Omega_{XA} = 80 \times 10^{12}$ s^{-1}. The calculations are numbered according to the success that was achieved in the optimization (see top panel in the figure). From figure 8 we conclude that all solutions that approach the maximum observed population are highly correlated. An inspection of the calculations reveals that all of these solutions are very close to a single Fourier-limited laser pulse. Deviations from the Fourier-limited pulse not only lead

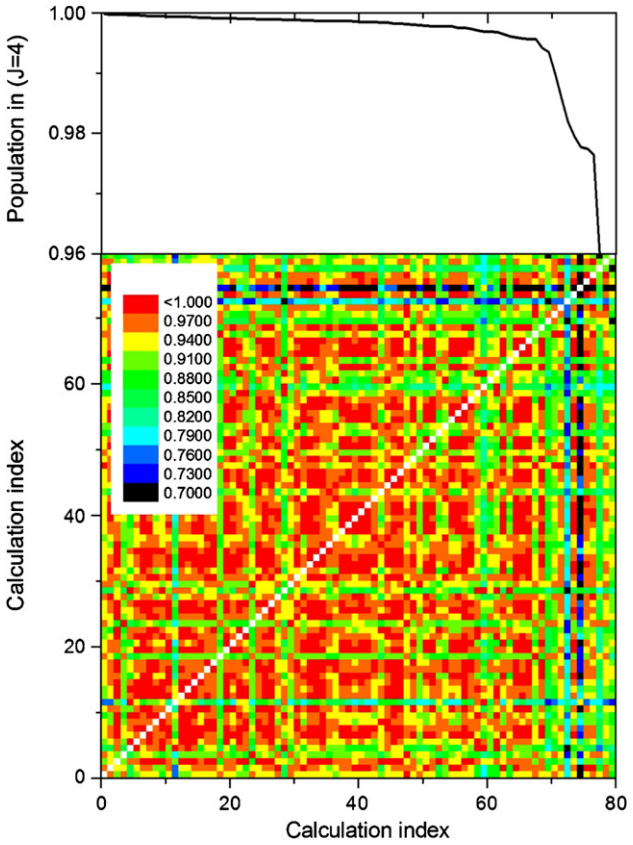

Figure 9. Population transfers from $J = 0$ to $J = 4$ obtained in 80 optimizations performed with the DR2 algorithm with $\Omega_{XA} = 120 \times 10^{12}\ s^{-1}$ (top), along with the correlation coefficient between these solutions, as defined by equation (8) (bottom). The solutions that perform well can be divided into a finite group of solutions that are highly correlated within the group but not with solutions outside the group. Pixels in white correspond to cross-correlation which (after rounding off) are equal to 1.

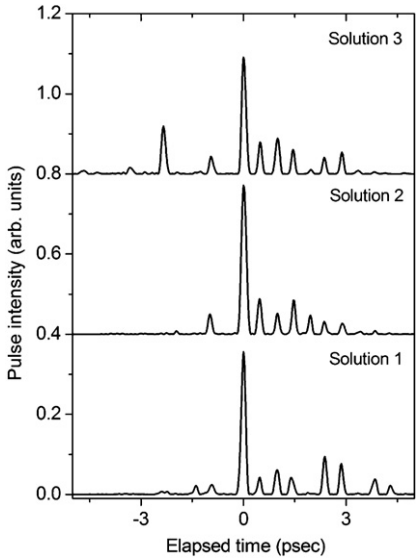

Figure 10. Comparison of the three best-performing pulse shapes that were obtained in 80 optimizations of the $J = 0 \rightarrow J = 4$ population transfer employing the DR2 algorithm with $\Omega_{XA} = 120 \times 10^{12}\ s^{-1}$. All solutions consist of trains of pulses with a spacing of 4.79×10^{-13} s, which corresponds to the beating period between $J = 2$ and $J = 4$.

to a drop in the correlation coefficient, but also in the efficiency of the population transfer.

In figure 9, the correlation coefficient is plotted for the 80 optimizations that were performed for $\Omega_{XA} = 120 \times 10^{12}\ s^{-1}$. In this case, the laser pulse energy is sufficient to transfer population from $J = 0$ to $J = 4$ with near-unit efficiency. The best solutions, which have a population transfer efficiency of 99.982% and 99.98%, are only weakly correlated to each other and are only weakly correlated to most of the other solutions. Specifically, there are only 9 solutions among the set of 80 that share a correlation coefficient larger than 0.95 with solution number 1. Of the remaining solutions, many are strongly correlated with the 3rd-best solution to have come out of the optimizations, which has a population transfer efficiency of 99.975%: as many as 41 solutions share a correlation coefficient larger than 0.95 with solution 3. While the three good solutions 1, 2 and 3 are rather different from each other, they contain most of the dominant features of the identified optimized solutions. Solutions 1–3 are shown in figure 10. Despite their difference, all three solutions in figure 10 are dominated by a series of peaks with a separation

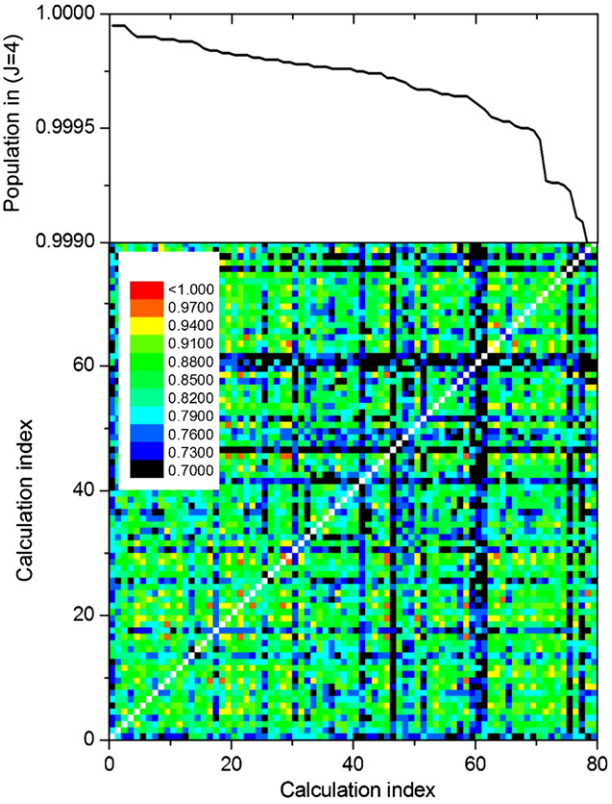

Figure 11. Population transfers from $J = 0$ to $J = 4$ obtained in 80 optimizations performed with the DR2 algorithm with $\Omega_{XA} = 160 \times 10^{12}\ s^{-1}$ (top), along with the correlation coefficient between these solutions, as defined by equation (8) (bottom). Many near-perfect solutions exist that are only weakly correlated to each other. Pixels in white correspond to cross-correlation which (after rounding off) are equal to 1.

of 4.79×10^{-13} s. This corresponds to the beating period of a coherent superposition of $J = 2$ and $J = 4$ ($\Delta E = 14B$). Additional good solutions likely exist, possibly continuously connected on a common level set, and further special numerical methods are needed to explore this possibility [40, 42].

In figure 11, the correlation coefficient is plotted for 80 optimizations that were performed for $\Omega_{XA} = 160 \times 10^{12}$ s^{-1}. While the degree of population transfer is very high in almost all the optimizations at this intensity, the correlation between the various solutions is very limited. Clearly, a large number of solutions that transfer the population with unit efficiency co-exist, with very little commonality between them. Indeed, inspection of pulse shapes obtained in the optimizations at $\Omega_{XA} = 160 \times 10^{12}$ s^{-1} reveals very complicated pulses, with few regular features, and an absence of the peak arising from coherence between $J = 2$ and $J = 4$ in the Fourier transform power spectrum.

In summary, upon increasing the intensity from $\Omega_{XA} = 80 \times 10^{12}$ s^{-1} to $\Omega_{XA} = 160 \times 10^{12}$ s^{-1} we find that population transfer is accomplished with an ever-increasing number of distinguishable solutions.

5. Conclusions and outlook

In the last few years, optimal control experiments using pulse shaping and a feedback loop governed by evolutionary algorithms have become a popular endeavour pursued by a rapidly increasing number of research groups worldwide. In the course of these efforts, the nature of the optimization process, the role of the pulse shaping device and the role of the optimization algorithm continue to be a source of lively discussion. The work here and elsewhere [39–41] shows that it is possible to encounter a high diversity of optimal solutions in constrained numerical simulations of quantum control and, moreover, that the examination of such rich sets of solutions can become an important aspect of the control experiments. The diversity of successful controls likely contains useful dynamical information and may also provide a list of choices to consider for weighing in other ancillary control criteria. The present calculations optimizing dynamic alignment and rotational population transfer in a diatomic molecule exposed to an intense, shaped laser field provide compelling evidence that the absolute value of the quantity that is being optimized (i.e., the 'fitness') is the true measure of success and that the same value of the fitness may be achievable by widely differing laser pulse shapes that share only a limited number of common features. Furthermore, the results presented here can be viewed as being the equivalent of the results reported by Rabitz *et al* in [13], where it was proved that controllable quantum systems with no constraints placed on the controls only have extrema that correspond to perfect control or to no control at all; additional analysis revealed the fundamental nature of control level sets [40–42] at the absolute extrema and at sub-optimal control yields. We also showed that the optimized alignment yield attained a value which was very close to the maximal possible yield in the current framework, even when the constraints on the optimization translated into a significant distortion of the resultant wave packet. By relaxing specific constraints, we showed that it was possible to enhance the observable alignment further towards the maximal attainable alignment possible for the rotational basis set used. This outcome leads to the optimistic conclusion that high yields may be obtained, even when *a priori* it seems that the system is subject to severe constraints for constructing the wave packet. The origin of this behaviour can be understood in terms of the variational principle as well as the physical observable involving an integration over the wavefunction which hides some of its discrepancies.

A striking aspect of the results is the evidence that the number of independent solutions produced by an optimization seems to critically depend on the difficulty of the problem. In the population transfer calculations we observed that at low intensity, where reaching the target is a hard problem with less than perfect yield, the trials invariably converge onto one and the same solution, whereas at higher intensity, where this represents an easier problem, a wide variety of solutions are encountered. Each of these solutions has the potential of carrying valuable information about the underlying physics, as we have observed in the case of optimization of field-free molecular alignment, where some of the solutions provided key information on the dynamics of the alignment process. Viewed in this sense, the uniqueness of the fitness value, and the diversity of the solutions that can lead to accomplishment, are blessings in disguise.

Acknowledgments

This work is part of the research program of the 'Stichting voor Fundamenteel Onderzoek der Materie (FOM)', which is financially supported by the 'Nederlandse organisatie voor Wetenschappelijk Onderzoek (NWO)'. HR acknowledges support from the DOE.

References

[1] Shapiro M and Brumer P 2000 *Adv. At. Mol. Opt. Phys.* **42** 287
[2] Mauritsson J *et al* 2006 *Phys. Rev. Lett.* **97** 013001
[3] Tannor D J and Rice S A 1988 *Adv. Chem. Phys.* **70** 441
[4] Vogt G *et al* 2006 *Chem. Phys. Lett.* **433** 211
[5] Vitanov N V *et al* 2001 *Ann. Rev. Phys. Chem.* **52** 763
[6] Judson R S and Rabitz H 1992 *Phys. Rev. Lett.* **68** 1500
[7] Assion A *et al* 1998 *Science* **282** 919
[8] Levis R J, Menkir G M and Rabitz H 2001 *Science* **292** 709
[9] Brixner T *et al* 2001 *Nature* **414** 57
[10] Herek J L *et al* 2002 *Nature* **417** 533
[11] Bartels R *et al* 2000 *Nature* **406** 164
[12] Zamith S *et al* 2004 *Phys. Rev.* A **70** 011201
[13] Rabitz H A, Hsieh M M and Rosenthal C M 2004 *Science* **303** 1998
[14] Weiner A M 2000 *Rev. Sci. Instrum.* **71** 1929
[15] Vaughan J C *et al* 2006 *Opt. Exp.* **14** 1314
[16] Rosca-Pruna F and Vrakking M J J 2001 *Phys. Rev. Lett.* **8715** 153902
[17] Meijer A S *et al* 2007 *Phys. Rev.* A **76** 023411
[18] Gijsbertsen A *et al* 2007 *Phys. Rev. Lett.* **99** 213003
[19] Stapelfeldt H and Seideman T 2003 *Rev. Mod. Phys.* **75** 543
[20] Friedrich B and Herschbach D 1995 *Phys. Rev. Lett.* **74** 4623
[21] Larsen J J *et al* 1999 *J. Chem. Phys.* **111** 7774

[22] Itatani J *et al* 2004 *Nature* **432** 867
[23] Kanai T, Minemoto S and Sakai H 2005 *Nature* **435** 470
[24] Leibscher M, Averbukh I S and Rabitz H 2003 *Phys. Rev. Lett.* **90** 213001
[25] Leibscher M, Averbukh I S and Rabitz H 2004 *Phys. Rev.* A **69** 013402
[26] Bisgaard C Z, Viftrup S S and Stapelfeldt H 2006 *Phys. Rev.* A **73** 053410
[27] Siedschlag C *et al* 2006 *Opt. Commun.* **264** 511
[28] Pinkham D, Mooney K E and Jones R R 2007 *Phys. Rev.* A **75** 013422
[29] Hertz E *et al* 2007 *Phys. Rev.* A **75** 031403
[30] Rosca-Pruna F and Vrakking M J J 2002 *J. Chem. Phys.* **116** 6579
[31] Shir O M *et al* 2006 *Artif. Evol.* **3871** 85
[32] Shir O F and Back T 2006 *Parallel Problem Solving from Nature—PPSN IX, Proc.* vol 4193 p 142
[33] Shir O M *et al* 2006 *Intelligent Data Engineering and Automated Learning—Ideal 2006, Proc.* vol 4224 p 410
[34] Shir O F *et al* 2006 *Proc. GECCO'06* (New York: ACM)
[35] Shir O F *et al* 2007 *Gaining Insight into Laser Pulse Shaping by Evolution Strategies* (Berlin: Springer)
[36] Beyer H-G and Schwefel H-P 2002 *Nat. Comput.* **1** 3
[37] Hansen N and Ostermeier A 2001 *Evol. Comput.* **9** 159
[38] Ostermeier A, Gawelczyk A and Hansen N 1994 *Parallel Problem Solving from Nature (PPSN)* vol 866 p 189
[39] Mitra A and Rabitz H 2004 *J. Phys. Chem.* A **108** 4778
[40] Rothman A, Ho T S and Rabitz H 2006 *Phys. Rev.* A **73**
[41] Roslund J, Roth M and Rabitz H 2006 *Phys. Rev.* A **74**
[42] Beltrani V *et al* 2007 *J. Chem. Phys.* **126**